Aerodynamic explanation of flight speed limits in hawkmoth-like flapping-wing insects

Seth Lionetti,[1] Tyson L. Hedrick ●,[2] and Chengyu Li ●[1,*]

[1]*Department of Mechanical Engineering, Villanova University, Villanova, Pennsylvania 19085, USA*
[2]*Department of Biology, University of North Carolina at Chapel Hill, Chapel Hill, North Carolina 27599, USA*

The hawkmoth is able to sustain a steady hover or level flight at lower speeds. However, previous wind tunnel experiments have suggested that long sequences of steady forward flight are less common at higher flying speeds (> 4.0 m/s) despite changes to the flight posture. This flying speed is about one-half of the theoretical prediction based on its body mass. It is unclear why hawkmoths have not been observed achieving steady flight at higher speeds. This paper aims to compare the aerodynamics involved in hawkmoth hovering to those in forward flight. High-speed video recordings and three-dimensional surface reconstruction were used to capture a hawkmoth's wing kinematics when hovering and at forward flight speeds of 2 and 4 m/s. Following reconstruction, the insect model was simulated using an in-house immersed-boundary-method based computational fluid dynamics (CFD) solver. The CFD solver provided a quantitative measure of the force generation, power consumption, and vortex structures generated during sustained flight. These results enabled the analysis of certain trends in how a hawkmoth adjusts flapping kinematics and its associated unsteady aerodynamics changes across different flight speeds. The results show that the moth minimizes drag as flying speed increases, but it immediately loses its lift producing upstroke even at the slow forward flight speed (2 m/s). A significant amount of negative lift is generated during upstrokes at the high forward flying speed (4 m/s). This negative lift in the upstroke potentially reduces maximum sustained flight speeds. This paper provides physical insight into the low-speed flights in flying insects.

I. INTRODUCTION

As insects flap their wings, they create a tornado-shaped leading-edge vortex (LEV) above the wing surface to generate sufficient aerodynamic force required to perform various flight tasks [1]. As a consequence, the unsteady flow evolves to a trail of aerodynamic footprints (complex vortex structures) in the wake. Among all flight modes, the two most widely studied modes are hovering and forward flight due to their potential broader applications in man-made robotic designs. In order to achieve a sustained flight mode at a fixed position (hovering) or at a constant forward flight speed (cruising), insects need to adjust their wing movements to reach a force balance in both vertical and horizontal directions.

Previous studies have used several different methods to examine how insects' kinematics and aerodynamics change as their flight speed increases. Dudley and Ellington [2,3] used high-speed cinematography and a force transducer to measure bumblebee wing kinematics and aerodynamic performance over a range of flight speeds (0–4.5 m/s). They found that as a bumblebee's forward flying speed increases, its wing angle of attack relative to the stroke plane also increases. In addition,

---

*chengyu.li@villanova.edu

during hovering flight, the bumblebee's downstroke and upstroke were shown to provide equal contributions to its total lift. However, as the bumblebee transitions to forward flight, its downstroke plays an increasingly dominant role in lift production. Zhu and Sun [4] demonstrated a similar trend using computational fluid dynamics (CFD) simulations of fruit fly forward flight. Results showed that as a fruit fly's flight speed increases, its stroke plane becomes more vertical, and its wing angle of attack during the upstroke increases. In addition, a fruit fly's downstroke contributes approximately half of the total lift at low forward flying speeds, whereas at high forward flying speeds, the downstroke contributes almost all of the total lift. Song and co-workers [5,6] also performed CFD simulations of hummingbird hovering and fast forward flight. Results showed that during hummingbird hovering, lift production is asymmetric between the downstroke and the upstroke with the downstroke producing 74% of the total lift, consistent with particle imaging velocimetry results [7]. During hummingbird fast forward flight, the downstroke contributes all of the total lift, and negative lift is generated during the upstroke. Song and co-workers suggest that at high hummingbird forward flying speeds, the upstroke is used to generate thrust at the cost of lift production. In a separate study, Suzuki *et al.* [8] simulated forward flight of a butterflylike flapping model with various flapping kinematics and Reynolds numbers. Their parametric study demonstrated most of the lift force was generated during the downstroke. The backward flapping motion during the upstroke created a significant negative lift force, and the magnitude of the negative lift could be modified by tuning the maximum angle of attack of flapping cycle.

The hawkmoth is another small flying animal capable of both hovering and forward flight. Hedrick and Daniel [9] discovered many different sets of kinematic parameters capable of producing hovering flight in a model hawkmoth. Their results suggest that the flapping mechanism used in hawkmoth flight is likely determined by factors beyond kinematic and aerodynamic performance. These factors may include biological constraints, such as the ability to apply a single wing beat pattern to several different flight modes. For a flying animal of its size, a hawkmoth's maximum forward flying speed has been reported much lower than expected. Stevenson *et al.* [10] used the hawkmoth's body mass to calculate a theoretical maximum flying speed of 7–10 m/s. However, experimental results have shown that hawkmoths are incapable of sustaining steady forward flight at speeds greater than 5 m/s [11,12]. Studying how a hawkmoth's wing kinematics and aerodynamics change as its flight speed increases can help explain why its maximum forward flying speed is lower compared to other flying animals with similar body mass, such as hummingbirds. Willmott and Ellington [11] used high-speed videography to calculate a hawkmoth's wing kinematics for flight speeds ranging from 0 m/s (hovering) to 5 m/s (forward flight). Results showed that as the hawkmoth's flying speed increased, its stroke plane angle became more vertical. This trend is consistent with the previously discussed results for other flying animals. Willmott and Ellington [13] also studied the aerodynamic performance of hawkmoths flying over the same range of speeds. They used a modified blade-element (BEM) approach to calculate the mean lift and drag coefficients for stationary hawkmoth wings. Because the wings were stationary, a time history of the instantaneous lift and drag was not provided. In addition, the researchers were able to qualitatively determine that the downstroke increasingly dominates lift support as forward flying speed increases, but exact contributions were not calculated in their study.

In addition to the above experimental measurements, Aono *et al.* [14] used real insect data to perform CFD simulations of hawkmoth hovering. The researchers noted the formation of a doughnut-shaped vortex ring in the wake of the hovering hawkmoth. Their results showed that the downstroke and upstroke both provided significant contributions to the total lift, but simulations for hawkmoth forward flight were not part of this paper. Zheng *et al.* [15] also used real hawkmoth hovering data to compare CFD simulation results with a BEM-based approach. Results showed that the BEM approach did not match the predictive abilities of the CFD. The researchers also found that for hawkmoth hovering, most of the lift is generated during the downstroke, similar to results from hummingbirds. This paper also did not include any simulations of hawkmoth forward flight. Yao and Yeo [16] performed CFD simulations of both hawkmoth hovering and forward flight. However, wing kinematics were prescribed using a generic proportional-integral-derivative controller and were not

based on real hawkmoth flapping data. Results from this paper showed that for hawkmoth hovering, the downstroke and upstroke provided approximately equal contributions to the total lift generated during each wing beat. At a forward flying speed of 1.3 m/s, the downstroke provided most of the lift, but positive lift was still generated during the upstroke. At all flight speeds greater than 1.3 m/s, the upstroke generated negative lift. Yao and Yeo [16] suggest that this trend is due to the highly vertical stroke plane at high forward flying speeds.

As described above, prior experimental measurements and computational simulations of hawkmoth flight have mainly focused on hovering. The exception, Yao and Yeo [16], performed CFD simulations of hawkmoth forward flight but used a flat-plate wing with flapping kinematics prescribed as sinusoidal equations. The present paper is among the first to use real hawkmoth flight data to simulate hawkmoth flight over a range of flying speeds. We aim to find out what prevents the hawkmoth from achieving a fast forward flying from a fluid dynamics perspective. In the current paper, hawkmoth wing kinematics were reconstructed based on high-speed video recordings of flying hawkmoths at speeds of 0, 2, and 4 m/s in a wind tunnel. The reconstructed hawkmoth model was then simulated using an in-house immersed boundary method (IBM) based in-house CFD solver. Simulation results were used to calculate instantaneous lift and drag forces produced by the flying hawkmoth, and power consumptions required to achieve different flight motions. The force generation on the deformable wing surfaces and its associated near and far wake structures were compared across different flying speeds.

II. METHODOLOGY

A. Experimental setup and filming procedures

Hawkmoths were recorded flying at three different flight speeds-hovering (0 m/s), slow forward flight (2 m/s), and fast forward flight (4 m/s). Moths were males acquired as pupae from the domestic colony in the Department of Biology at the University of North Carolina at Chapel Hill. Following eclosure, moths were placed in individual $30 \times 30 \times 30$-cm-mesh cages in an environmental chamber maintaining $\sim 25\,°$C and a 20:4 light/dark cycle. Before filming, moths were not fed for a minimum of 12 h. At recording, each moth was placed inside a wind tunnel (octagonal working section, 1.2-m long and 0.6-m diameter, see Ortega-Jimenez *et al.* [17] for further details), and an artificial flower with a 1:4 honey:water mix was provided for the insect to feed on; moths were trained via prior experience to recognize the flower and feed from it at a variety of tunnel flow speeds. Three high-speed cameras (two Phantom v7.1 equipped with 35-mm Nikon lenses, and one Phantom v5.1 with a Zeiss 50-mm lens, Vision Research Inc., Wayne, NJ, USA) operating at 1000 frames s^{-1} with a 300 μs shutter duration were used to record hawkmoth flight. Illumination for the cameras was provided by four 12 W multi-light-emitting diode infrared (730-nm) lights (Larson Electronics LLC, Kemp, TX, USA); these emit at a wavelength below the hawkmoth visual spectrum and, thus, do not alter flight behavior. The cameras were calibrated for three-dimensional (3D) kinematics using a structure-from-motion approach [18]. During the experiments, the flight speed is controlled by changing wind tunnel speeds without removing the animal. Recordings from a single individual flying at different flight speed were selected for detailed 3D reconstruction and meshing for computational simulation. The morphological data for the hawkmoth used in this paper is summarized in Table I. Note that the moth was allowed to hover and feed to satiation after the video data were collected, and the prefeeding mass from Table I is expected to be characteristic of the moth during recordings. The flight speeds were recorded in the following order: 2, 4, and 0 m/s.

B. Reconstruction of hawkmoth flight

After recording hawkmoth hovering (0 m/s), 2-m/s forward flight, and 4-m/s forward flight, a meshed model of the flying hawkmoth was reconstructed using Autodesk Maya. In nature, hawkmoths possess both a forewing and a hind wing that combine to provide a lifting surface. However, in this paper, we joined the forewing and hind wing into a single mesh to reduce

TABLE I. Morphological data for the hawkmoth in this paper. The data for the wing is presenting a single side wing combining both forewing and hindwing.

Parameter	Values
Body mass before feeding (g)	1.45
Body mass after feeding (g)	1.95
Body length (cm)	5.3
Wing mass (g)	0.0382
Wing span length, R (cm)	5.5
Mean wing chord, c (cm)	2.3
Wing area (cm^2)	10.7
Flapping frequency, f (Hz)	27.9 ± 2.4

computational complexity. The computational wing used in our simulations is shown on the left in Fig. 1. The model hawkmoth was superimposed over the side-view and top-view high-speed video recordings of hawkmoth flight. For each flying speed, one flapping cycle was selected where the hawkmoth body was relatively stationary. At various points throughout the selected wing beat cycle, and the morphology of the model hawkmoth's left wing was adjusted to align with the high-speed recording. The flapping wings of the hawkmoth were reconstructed using a template-based hierarchical subdivision surface method [19,20]. Using easily identifiable natural patterns on the wing surfaces, we reconstructed the 3D wing kinematics with surface deformation during the flapping wing beat cycles. During the reconstruction process, we adjusted the subdivision control points to incorporate these natural twisting/bending deformations. As shown in the high-speed video recordings (included in the Supplemental Material [21]), the hawkmoth's wings bend and twist considerably during flight. Between these reconstructed points, Fourier interpolation was used to reconstruct hawkmoth flapping motions. A side-by-side comparison between high-speed video recording and reconstructed model is demonstrated in the Supplemental Material [21].

Using the reconstructed data, the hawkmoth's body incline angle and stroke plane angle were determined for each flight speed. As shown in Fig. 2, the body incline angle is defined as the angle between the hawkmoth body and the horizontal x axis. The stroke plane angle is defined as the angle between the stroke plane and the x axis. The stroke plane was determined based on the least-squares plane of the wingtip trajectory that passes through the wing root and is represented by the dashed line in Fig. 3. Next, wing kinematics were quantified on the stroke plane using three Euler angles: wing stroke (ψ), wing deviation (ϕ), and wing pitch (θ). The wing stroke angle provides the location of the wing in the stroke plane, defined as the angle between the projection of the root-to-tip connection line and the z axis. The deviation angle is the angle between the line from wing root to tip and its projection onto the stroke plane. The wing pitch angle provides the angle between the wing chord and the stroke plane.
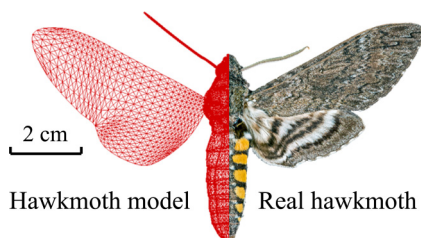

2 cm

Hawkmoth model   Real hawkmoth

FIG. 1. Comparison between the hawkmoth meshed model and the real hawkmoth. The hawkmoth mesh shown on the left was used for all simulations in this paper.
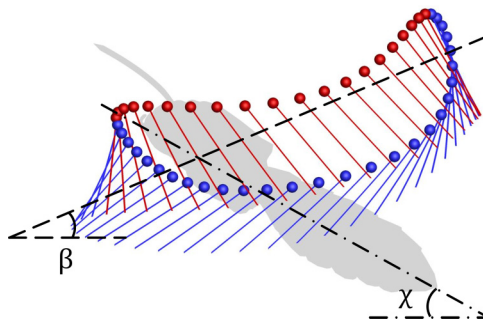
FIG. 2. Definition of stroke plane angle (β) and body incline angle (χ). Colored circles in the figure denote the wing leading edge, and the lines present the pitch angle of wing chord at the 0.75R along the wingspan. The hawkmoth flapping motion follows a counterclockwise trajectory. The downstroke is pictured in red, and the upstroke is shown in blue. See movie 1 in the Supplemental Material for reconstructed flapping motions [21].

C. Governing equations and numerical method

The numerical methodology of the immersed-boundary-method-based in-house CFD solver employed in the current paper is briefly introduced here. The 3D viscous incompressible Navier-Stokes equations can be written in a tensor form as follows:

$$\frac{\partial u_i}{\partial x_i} = 0, \quad \frac{\partial u_i}{\partial t} + \frac{\partial (u_i u_j)}{\partial x_j} = -\frac{\partial p}{\partial x_i} + \frac{1}{\mathrm{Re}} \frac{\partial}{\partial x_j} \left(\frac{\partial u_i}{\partial x_j} \right), \tag{1}$$

where u_i are the velocity components, p is the pressure, and Re is the Reynolds number.

The above equations are discretized using a cell-centered collocated arrangement of the primitive variables and are solved using a finite difference-based Cartesian grid immersed-boundary method [22]. The equations are integrated in time using the fractional step method. A second-order central difference scheme is employed in space discretization. The Eulerian form of the Navier-Stokes equations is discretized on a Cartesian mesh and boundary conditions on the immersed boundary are imposed through a ghost-cell procedure. Compared to the boundary-conforming methods, such
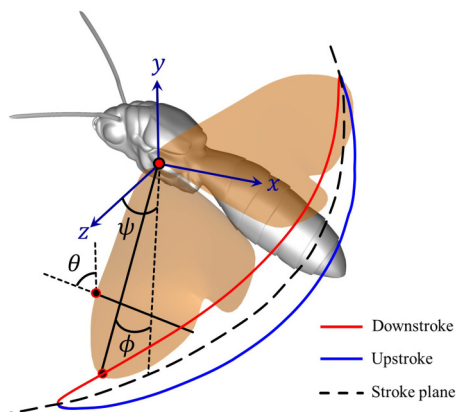

FIG. 3. Wing Euler angles definition, including wing stroke (ψ), wing deviation (ϕ), and wing pitch (θ) angles. The wingtip trajectory during the downstroke is shown in red, and the upstroke is shown in blue. Two snapshots of the left hawkmoth wing are shown—one at the beginning of the flapping cycle and one during the downstroke.
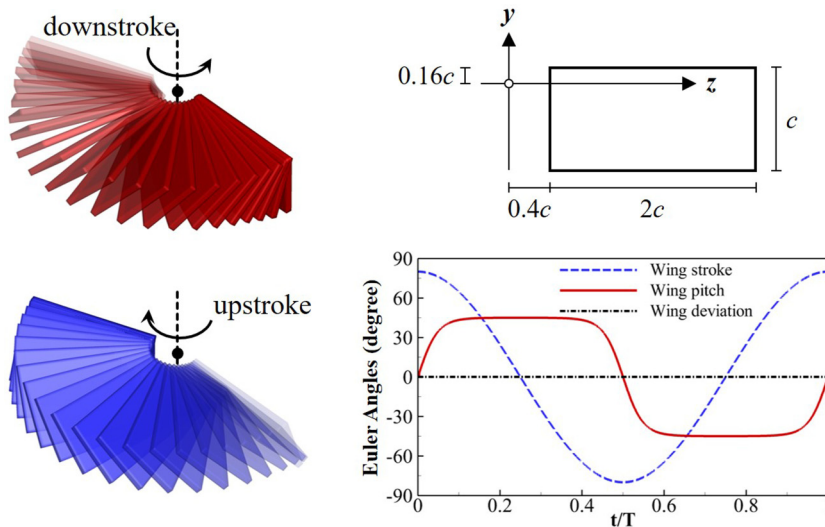
FIG. 4. Wing kinematics of a rectangular flapping wing used in solver validation. The benchmark setup is based on Suzuki *et al.* [8].

as the curvilinear grid [23–25] and the finite-element methods [26–28], the IBM approach eliminates the need for complicated remeshing algorithms. It, thus, significantly reduces the computational cost associated with simulating flow past complex moving boundaries. Immersed boundary methods can be broadly characterized under two categories: continuous forcing approach [29–31] and discrete forcing approach [32–34]. The present paper employs a multidimensional ghost-cell methodology to impose the boundary conditions on the immersed boundary [22]. This method can be categorized as a discrete forcing approach wherein forcing is directly incorporated into the discretized Navier-Stokes equations [35]. The movement of the immersed boundaries (hawkmoth wings) were prescribed according to the image-based reconstruction. This method has been successfully applied in the simulations of insect flights [36–38] and bioinspired propulsions [39–42]. Validations of the current in-house CFD solver can be found in our previous studies [20,43–45].

D. Validation of computational modeling

1. Flapping rectangular wing

To demonstrate the validity of the CFD solver, a benchmark setup proposed by Suzuki *et al.* [8] is used here. The simulation consists of a rectangular wing flapping along a horizontal stroke plane with zero deviation (Fig. 4). The rectangular wing has a chord length c, a spanwise length $L = 2c$, and a thickness of $w = 0.1c$. The wing kinematics are controlled by two rotational angles: wing stroke and wing pitch. The wing stroke angle provides the location of the wing on the stroke plane and is prescribed by $\psi(t) = \psi_m \cos(2\pi f t)$, where $\psi_m = 80°$. For the wing rotation along the stroke plane, the wing root is extended out at a distance $0.4c$ away from the vertical rotational axis. The wing pitch angle is given by $\theta(t) = \theta_m \tanh[C_\eta \sin(2\pi f t)]/\tanh(C_\eta)$ in which $\theta_m = 45°$ and $C_\eta = 3.3$. The rotational axis of wing pitch is located at a distance $0.16c$ from the wing's leading edge. The Reynolds number ($\mathrm{Re} = \overline{U}_{\text{tip}} c / v$) is set to 100 in which the average tip velocity is calculated by $\overline{U}_{\text{tip}} = 2\pi f \psi_{\text{m}}(L + 0.4c)$. A nonuniform Cartesian grid of size $305 \times 137 \times 177$ is used in a computational domain of size $30c \times 30c \times 30c$ to get domain independence results. The simulation is conducted for four flapping cycles. The lift coefficient is calculated by $C_L = 2F_L/(\rho \overline{U}_{\text{tip}}^2 L c)$, and the drag coefficient is calculated by $C_D = 2F_D/(\rho \overline{U}_{\text{tip}}^2 L c)$. Figure 5 shows the lift and drag
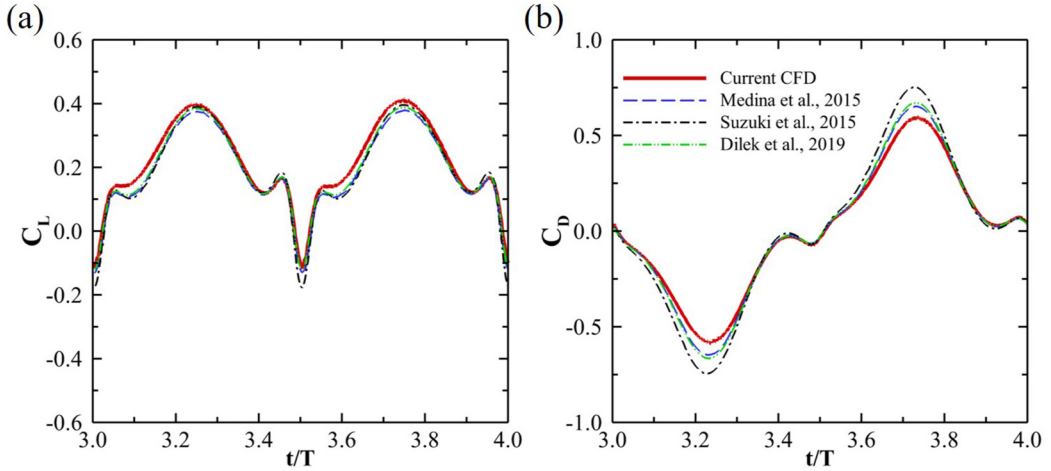
FIG. 5. Comparison of lift (a) and drag (b) coefficients of flapping rectangular wing between current CFD results and data available in the literature [8,46,47].

coefficients from the fourth cycle together with the simulation results from the literature [8,46,47]. As can be seen, our simulation results capture the key features of the instantaneous forces well and present good agreement with the simulation data from the literature.

2. Hovering hawkmoth

In addition to the flapping rectangular wing, the aerodynamic force production of the hovering hawkmoth was compared to previous studies. A reconstruction of hovering hawkmoth flight was created, and the model was immersed in a nonuniform Cartesian computational grid with size $225 \times 193 \times 225$. Following the simulation, aerodynamic lift and drag production was calculated for both wings and the hawkmoth's body. Figure 6 compares our CFD results with the forces
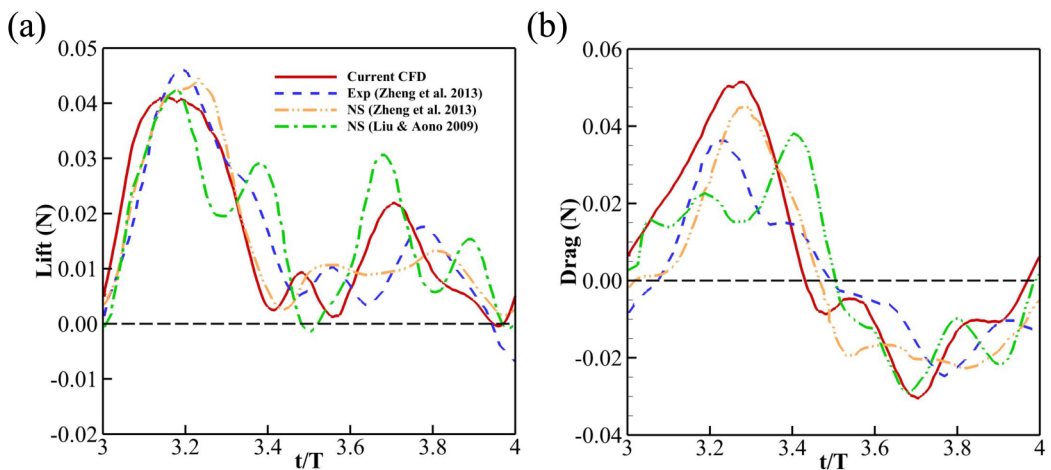

FIG. 6. Validation of the in-house CFD solver used in this paper. Lift and drag forces produced by a hawkmoth's wings and body in hovering flight are plotted against previous experimentally and computationally determined results. Experimental and numerical results obtained by Zheng *et al.* [15] and Aono *et al.* [14] are included.
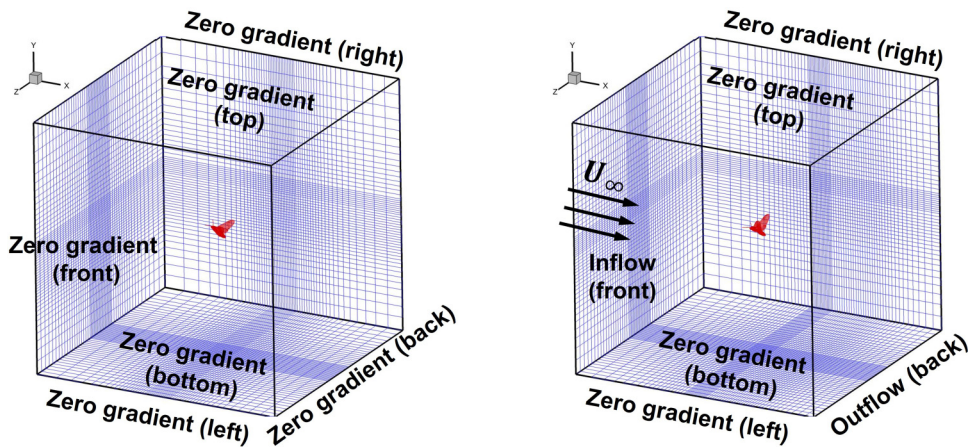
FIG. 7. Simulation setup and computational grids applied in the paper. Grids are shown for hovering (left) and forward flight (right).

calculated by Zheng *et al.* [15] using both numerical and experimental approaches. In addition, the numerical results obtained by Aono *et al.* [14] are also included. As illustrated in Fig. 6, the force magnitudes and overall trend of our calculations are consistent with the literature. Specifically, the force predictions from the current paper are aligned best with the experimental estimation of aerodynamic forces calculated in the study of Zheng *et al.* [15]. It is worth noting that there is some variation between the different studies presented in Fig. 6. The discrepancies can be explained by the fact that different hawkmoths were used in each study. Natural variations in wing shape, body size, and flapping kinematics between different individual hawkmoths can lead to slight differences in force magnitude. Despite these differences, the overall trend of force production in the current paper is consistent with previous results. Additional validations of the current in-house solver can be found in our previous studies [20,36,40,43,45].

E. Simulation setup

Figure 7 shows the simulation setup for both hovering and forward flight. The domain mesh has two refined layers. As seen in this figure, a very high-resolution mesh is provided in a rectangular region around the hawkmoth. Around this region, there is a secondary denser mesh, and beyond this layer, the grid is stretched rapidly. Different computational grids were used for hovering and forward flight to accommodate different relative positions of downwash. In addition, different boundary conditions were also applied to the two meshes. For hovering, a zero gradient was used for all boundaries. For forward flight, the inflow boundary condition was specified at the front of the fluid domain, and an outflow boundary condition was used at the back of the fluid domain. At all other boundaries, a zero gradient was adopted. The forward flight grid contains approximately one million more computational cells than the grid used for hovering flight. In order to achieve a periodic state of the force history, all simulations were run for four flapping cycles. We concluded that the force history was periodic after four flapping cycles because the difference in cycle-averaged lift between the third and fourth flapping cycles was very small ($<2\%$ for all three flight conditions). The simulation results we present in the results section are based on the fourth flapping cycle.

The simulations were carried out on a nonuniform Cartesian grid. The grid size employed in the current simulations is $225 \times 193 \times 225$ ($\Delta x \cong 0.0044R$) for hovering and $313 \times 153 \times 225$ ($\Delta x \cong 0.0041R$) for forward flight. To ensure the simulation results are grid-independent, grid independence studies were performed for both hovering flight and forward flight at 4 m/s. Figure 8 shows the comparison of simulated lift and drag for a single hawkmoth wing in three grids of
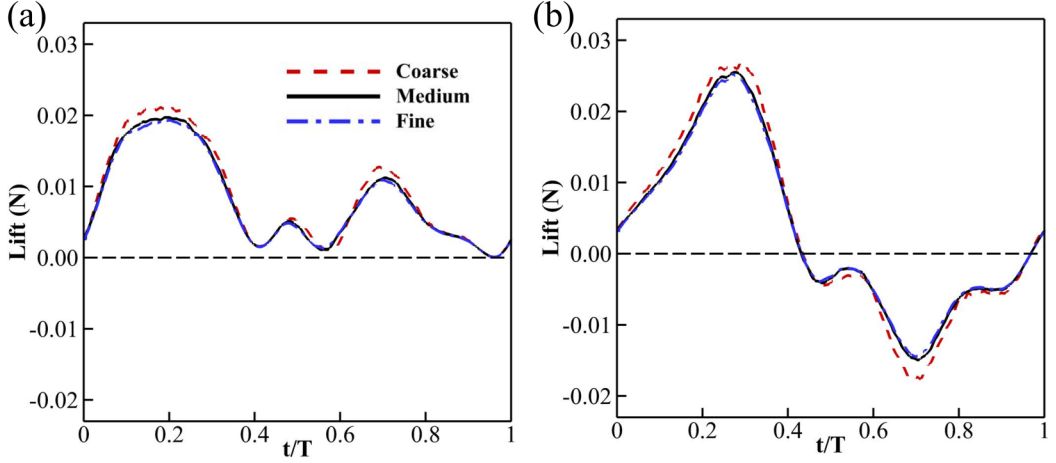
FIG. 8. Lift and drag force production during hovering flight by a single hawkmoth wing. Results are shown for three different grid densities: coarse ($177 \times 145 \times 177 \approx 4.5 \times 10^6$, $\Delta x \cong 0.0096R$), medium ($225 \times 193 \times 225 \approx 9.8 \times 10^6$, $\Delta x \cong 0.0044R$), and fine ($257 \times 225 \times 257 \approx 1.5 \times 10^7$, $\Delta x \cong 0.0019R$).

different densities at hovering. The coarse mesh presents slightly higher peak values for both lift and drag forces compared to other two meshes. This can partly be explained by the pressure oscillation of the immersed-boundary method when the mesh resolution is not sufficient for the moving boundaries. When the medium mesh is applied for the simulation, the difference between the cycle average force for the medium and fine meshes is less than 3% for both lift and drag, which indicates that grid-independent results are achieved.

In the present paper, we observed that the hawkmoth slightly changed its flapping frequency as the flying speed increased from 0 m/s (hovering) to 4 m/s (forward flight). In order to make a fair comparison, we incorporate both cycle-averaged wing-tip velocity and flight speed in the definition of Reynolds number. Following the previous literature [48], the Re and advance ratio (J) in our paper are defined as

$$\mathrm{Re} = \frac{(\bar{U}_{\mathrm{tip}} + U_\infty)c}{v} = \frac{(1+J)(2\Phi f R)c}{v}, \tag{2}$$

$$J = \frac{U_\infty}{\bar{U}_{\mathrm{tip}}} = \frac{U_\infty}{2\Phi f R}, \tag{3}$$

where U_∞ represents the body moving velocity (zero for the hovering case); $\bar{U}_{\mathrm{tip}}$ is the mean wing tip velocity and can be expressed as $2\Phi f R$ in which Φ is the stroke amplitude, f is the flapping frequency, and R is the wing root to tip length (0.055 m for all cases); c is the average wing chord length (0.023 m for all cases); and v is the fluid kinematic viscosity (around 1.56×10^{-5} m^2 s^{-1} for air at room temperature of 25 °C).

F. Evaluation of power consumption

In this paper, the mechanical power (P_{mech}) was calculated using a similar treatment as presented by Wan *et al.* [49] and Aono and Liu [50]. The mechanical power includes two components, namely, aerodynamic power (P_{aero}) and inertial power (P_{iner}). Specifically, the aerodynamic power is the power needed to overcome air resistance, and it is defined as the scalar products of the velocity and

the aerodynamic force of the wing [Eq. (4)],

$$P_{\text{aero}} = -\sum_i^N (F_{\text{aero,i}} v_i),\tag{4}$$

$$P_{\text{iner}} = \iint \bar{\rho}_w \bar{h} \frac{d\boldsymbol{u}_c}{dt} \cdot \boldsymbol{u}_c ds.\tag{5}$$

The inertial power is the power needed to accelerate each wing, and it is defined as the surface integral of the product of the average wing density, average wing thickness, acceleration of each element, and the velocity of each element [Eq. (5)]. In our calculation, the product $\bar{\rho}_w \bar{h}$ was calculated as the wing mass divided by the wing surface area (m_{wing}/S). The mechanical power required to move each wing is the sum of the aerodynamic power and the inertial power [Eq. (6)]. The power can be normalized by dividing by the body mass (m_b) of the hawkmoth to compute the mass-specific power [Eq. (7)],

$$P_{\text{mech}} = P_{\text{aero}} + P_{\text{iner}},\tag{6}$$

$$P^* = \frac{P_{\text{mech}}}{m_b}.\tag{7}$$

The true cycle-averaged mechanical power $\bar{P}^*$ depends on the elastic energy storage of the hawkmoth wings and, therefore, cannot be reported directly. Instead, limiting cases representing 0% and 100% elastic storage must be considered, and the real $\bar{P}^*$ lies between these values [51]. In the case of 0% elastic storage, all negative power is dissipated, and the cycle-averaged mechanical power can be written as

$$\bar{P}^*_{\text{mech},0\%} = \bar{P}^+.\tag{8}$$

In the case of 100% elastic storage, all negative power is stored for later use, and the cycle-averaged mechanical power can be written as

$$\bar{P}^*_{\text{mech},100\%} = \bar{P}^+ - |\bar{P}^-|.\tag{9}$$

III. RESULTS AND DISCUSSION

A. Flight kinematics at different flying motions

Figure 9 shows image sequences we collected in the experiments for the hawkmoth under hovering motion, 2-m/s forward flight, and 4-m/s forward flight over the course of one wingbeat cycle. Based on these images, it is clear that the hawkmoth's flight kinematics change substantially as the insect transitions from hovering to forward flight. During the hovering downstroke (approximately $t/T = 0.125$ to 0.5), the wings sweep horizontally past the body lateral center towards the front of the moth. This "back-and-forth" flapping behavior indicates a significant negative stroke angle as the hawkmoth begins the upstroke ($t/T = 0.5$) as defined in Fig. 3. At forward flying speeds, the hawkmoth transitions to a more "up-and-down" flapping motion. At 4-m/s forward flight, the wings do not reach to the body lateral center at all, resulting in a consistently positive stroke angle. In addition, during hovering flight, the hawkmoth's wings exhibit a significant pitching motion where they rotate to form an angle with respect to the stroke plane as defined in Fig. 3. The wing pitch during hovering flight is most clearly seen at $t/T = 0.5$ and 0.625 in Fig. 9. At higher flight speeds, however, the wing pitching motion is less pronounced with the wings remaining more horizontal throughout the flapping cycle. The hawkmoth's body angle also changes as its flight speed increases. At hovering, the body angle is significantly greater than during forward flight. In addition, Fig. 9 shows that at each flying speed, the upstroke begins roughly halfway through the flapping cycle. The duration of the upstroke and downstroke was determined by inspecting the high-speed video of the flying hawkmoth (included in the Supplemental Material [21]). Each half-stroke begins once
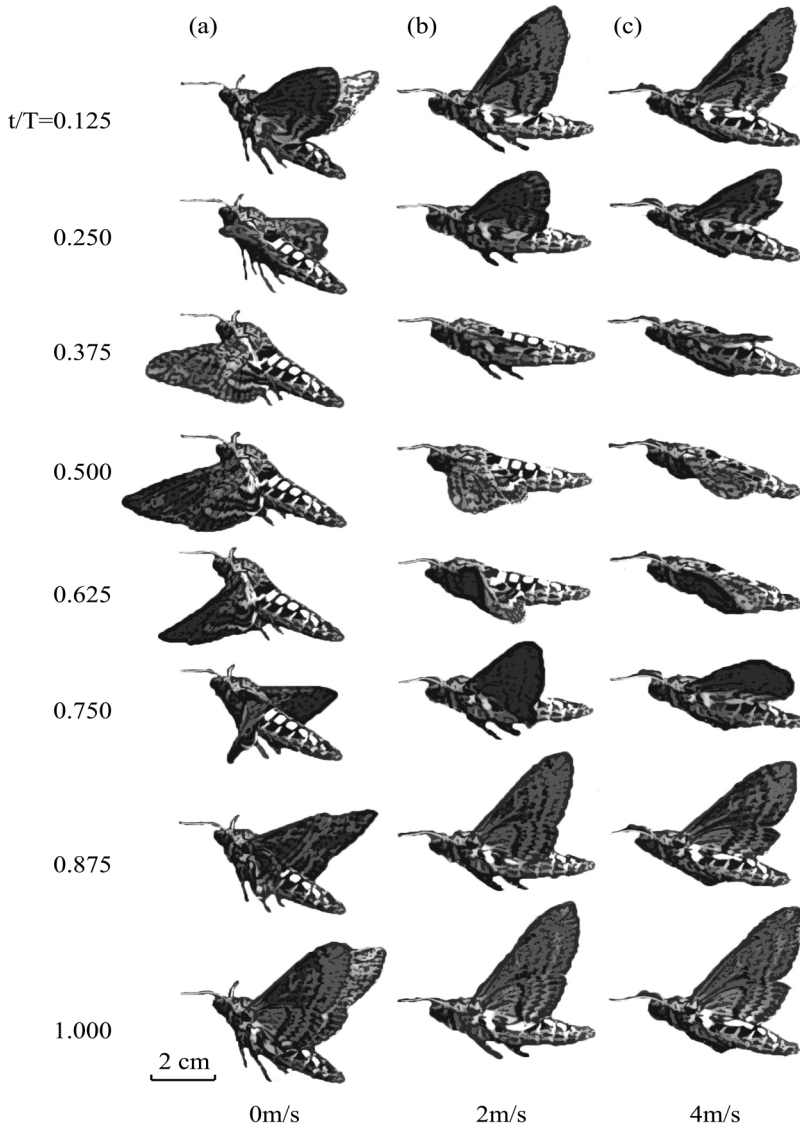
FIG. 9. Images of the hawkmoth while (a) hovering and at forward flight speeds of (b) 2 m/s and (c) 4 m/s. See movie 1 in the Supplemental Material for high-speed video recording [21].

the wingtip reverses direction at the end of the previous half stroke. For each flight speed, the downstroke comprises approximately 47% of the flapping cycle duration.

For each flight speed, the flapping cycle shown in Fig. 9 was used to calculate the wing Euler angles. Figure 10 shows the instantaneous Euler angles during one flapping cycle for hawkmoth hovering, 2-m/s forward flight and 4-m/s forward flight. The Euler angle plots in Fig. 10 reinforce the qualitative observations performed using Fig. 9. At hovering, the stroke angle ψ ranges from $50°$ at the beginning of the downstroke to $-50°$ at the beginning of the upstroke. This is evidence of the back-and-forth sweeping flight pattern depicted in Fig. 9. At 4-m/s forward flight, the stroke angle is consistently positive. This corresponds to the transition towards a more up-and-down flapping motion at higher flight speeds. Figure 10 also shows that the wing pitch angle tends to peak during the upstroke, and as flying speed increases, the maximum pitching angle decreases. The maximum
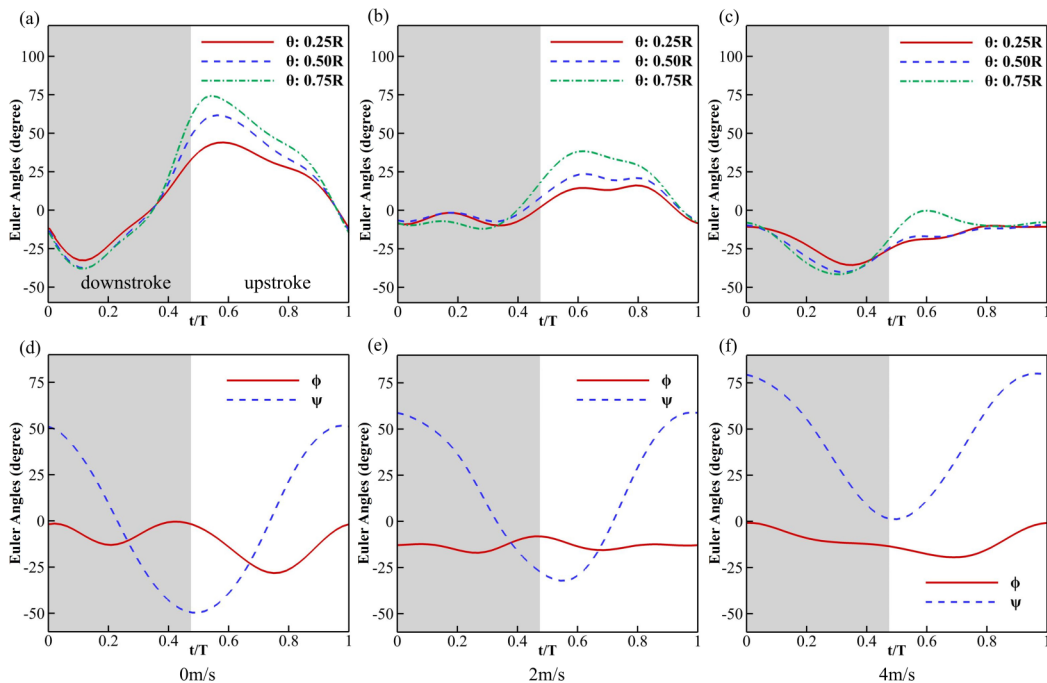
FIG. 10. Wing Euler angles for hawkmoth hovering (a) and (d), 2-m/s forward flight (b) and (e), and 4-m/s forward flight (c) and (f). The first row of plots shows the wing pitch (θ) angle at three different locations along the wingspan R. The second row shows the wing stroke (ψ) and wing deviation (ϕ) angles for each flight speed. The downstroke is shaded gray.

wing pitch angle at $0.50R$ decreases from $63°$ at hovering to $-10°$ at 4-m/s forward flight. This is evidence of the decrease in wing pitching motion observed using Fig. 9.

Figure 11 shows the hawkmoth's wing trajectory and wing chord orientation for hovering, 2-m/s forward flight and 4-m/s forward flight. During hovering flight, the wing chords are significantly more vertical than during 4-m/s forward flight. This is evidence that as the hawkmoth's flight speed increases, its wing pitch angle becomes more parallel to the incoming flow, which potentially reduces the drag force generated during the downstroke. Figure 11 also shows that the stroke plane angle for hawkmoth hovering is smaller than the stroke plane angle for both forward flying speeds. In addition, the body incline angle during hovering flight is greater than during forward flight.
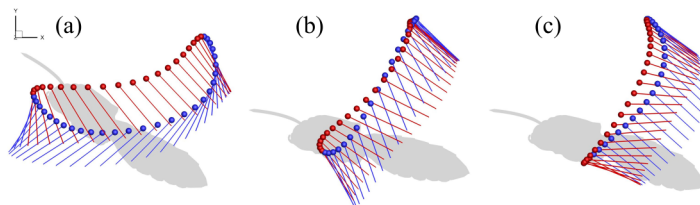

FIG. 11. Wing chord trajectory for (a) hawkmoth hovering, (b) 2-m/s forward flight, and (c) 4-m/s forward flight. Colored circles in the figure denote the wing leading edge, and the lines present the wing chord at the $0.75R$ along the wingspan. The hawkmoth flapping motion follows a counterclockwise trajectory. The downstroke is pictured in red, and the upstroke is shown in blue. See movie 1 in the Supplemental Material for reconstructed flapping motions [21].

TABLE II. Table summarizing significant wing kinematics parameters.

Parameter	Hovering	Slow forward flight	Fast forward flight
Avg. body moving velocity (U_∞)	0 m/s	2 m/s	4 m/s
Flapping frequency (f)	25.6 Hz	27.8 Hz	30.3 Hz
Stroke amplitude (Φ)	101.22°	91.09°	81.21°
Advance ratio (J)	0	0.41	0.85
Reynolds number (Re)	7335	10117	12863
Stroke plane angle	57.61°	72.54°	66.44°
Body incline angle	30.0°	14.0°	16.0°

We summarized the changes in significant kinematic parameters in Table II. Table II also includes the advance ratio J and Re for different flight speeds. These calculations rely on the flapping frequency f and the stroke amplitude Φ. The flapping frequency is equal to 25.6 Hz for hovering, and it increases to 27.8 and 30.3 Hz for 2- and 4-m/s forward flight, respectively. The stroke amplitude tends to decrease as flying speed increases. Table II also shows that the stroke plane angle for both forward flying speeds is greater than for hovering, but the stroke plane angle for 2-m/s forward flight is slightly greater than the stroke plane angle for 4-m/s forward flight. In addition, the body incline angle for forward flight is significantly smaller than the body angle for hovering, but the body incline angle for 4-m/s forward flight is slightly greater than the incline angle for 2-m/s forward flight.

B. Evaluation of unsteady aerodynamics of hawkmoth under various flight speeds

Using the reconstructed body and wing kinematics described in the previous section, the unsteady flow and its associated aerodynamic forces were captured using the in-house CFD solver. In Fig. 12, we compare the time history of lift (vertical force) and drag (horizontal force) forces on the hawkmoth body and left wing at different flying motions. The overall trend of lift and drag forces are significantly affected by the flying speed of hawkmoth. During hovering flight [Fig. 12(a)], the hawkmoth produces lift during both downstroke and upstroke with 72% of the lift being generated during the downstroke. However, as the hawkmoth transitions to forward flight, it loses its lift-producing upstroke. At flying speeds of 2 and 4 m/s, positive lift is only produced during the downstroke, and negative lift is generated during the upstroke. It is also worth noting that the lift force in the hovering case peaks three times throughout the flapping cycle: once during the downstroke, once during the transition from downstroke to upstroke, and once during the upstroke. However, during hawkmoth forward flight, the lift peaks only once at middownstroke [Figs. 12(b) and 12(c)]. For all three cases, the cycle-averaged lift generated by two wings matched reasonably well with the body weight of the hawkmoth (see Table III). As the hawkmoth switched from hovering to forward flight, its body also generated a small amount of lift due to the wing-body interaction [52], a contribution about one order of magnitude smaller than a single wing. In addition to keeping its body aloft in the air, another challenge for the flying hawkmoth is balancing its drag force along the horizontal direction [Figs. 12(d)–12(f)]. Although the cycle-averaged drag force is close to zero for all three cases, its magnitude is significantly different at various flying speeds. During hovering flight, the hawkmoth produces a large amount of positive drag during the downstroke and negative drag (thrust) during the upstroke. As the hawkmoth's flying speed increases, the magnitude of drag production is minimized. At 2 m/s, maximum drag production is 0.012N, roughly half the maximum drag during hovering. At 4-m/s forward flight, the drag force production during both downstroke and upstroke is almost negligible. We suspect that minimizing the drag force during the entire flapping cycle is critical to achieving stable fast forward flight for the hawkmoth. By modulating its flapping kinematics to achieve this, the hawkmoth inevitably produces
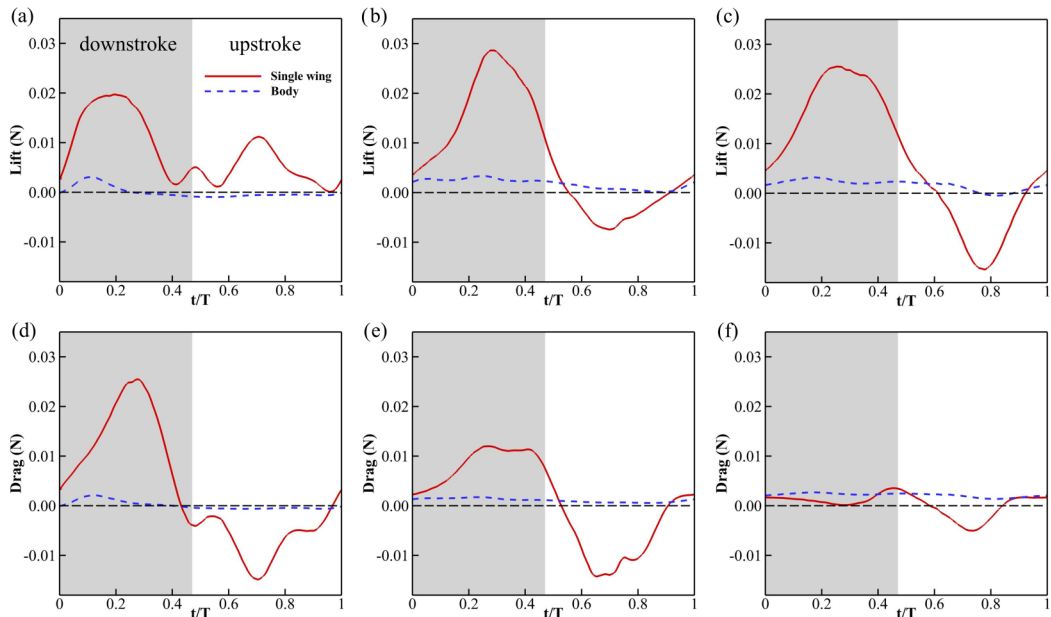
FIG. 12. (a)–(c) Lift and (d)–(f) drag force production for hawkmoth hovering, 2-m/s forward flight and 4-m/s forward flight. Force production is shown separately for a single hawkmoth wing and the hawkmoth body. The downstroke is shaded gray.

a large amount of negative lift during the upstroke. This biological limitation prevents the hawkmoth from reaching higher forward flying speeds as predicted based on its body size [10].

One may speculate that the flying speed limitation of hawkmoth observed in nature might be due to the high-power consumption in fast flight. In order to evaluate this possibility, we calculated the instantaneous mass-specific aerodynamic, inertial, and mechanical power for hawkmoth hovering, 2-m/s forward flight, and 4-m/s forward flight as shown in Fig. 13. This figure shows that for all flight speeds, the hawkmoth consumes more aerodynamic and mechanical power during the downstroke than during the upstroke. This is consistent with results previously obtained for other insects [49,51]. Greater power consumption during the downstroke is likely due to the downstroke's dominant role in lift production. Across all three flying speeds, most of the hawkmoth's lift is generated during the downstroke, resulting in greater power consumption. In addition, Fig. 13 shows

TABLE III. Cycle-averaged lift, mechanical power (with 100% elastic storage), lift-to-power ratio, mass-specific aerodynamic power ($\bar{P}^*_{\mathrm{aero}}$), inertial power ($\bar{P}^*_{\mathrm{iner}}$), 100% elastic mechanical power ($\bar{P}^*_{\mathrm{mech,100\%}}$), and 0% elastic mechanical power ($\bar{P}^*_{\mathrm{mech,0\%}}$) for hovering (0 m/s), slow forward flight (2 m/s), and fast forward flight (4 m/s).

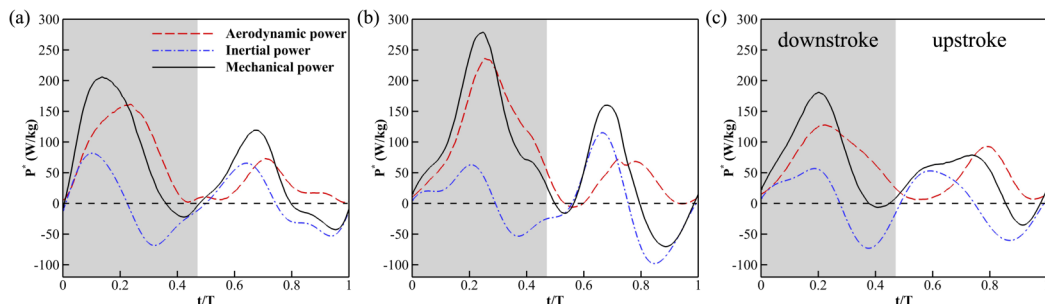| Cycle-averaged values	Hovering	Slow forward flight	Fast forward flight
Lift (mN)	16.38	16.09	15.22
Mechanical power (mW)	89.45	90.13	81.50
Lift-to-power ratio (N/W)	0.18	0.18	0.19
$\bar{P}^*_{\mathrm{aero}}$ (W/kg)	51.32	52.87	47.57
$\bar{P}^*_{\mathrm{iner}}$ (W/kg)	1.29	0.15	0.37
$\bar{P}^*_{\mathrm{mech,100\%}}$ (W/kg)	52.61	53.02	47.94
$\bar{P}^*_{\mathrm{mech,0\%}}$ (W/kg)	87.86	81.06	62.83

FIG. 13. Instantaneous mass-specific aerodynamic, inertial, and mechanical powers of wing pair for (a) hovering, (b) 2-m/s forward flight, and (c) 4-m/s forward flight. The downstroke is shaded gray.

that the inertial power is positive at the beginning of each half-stroke and negative towards the end of each half-stroke. As a result, the mechanical power briefly becomes negative before each stroke reversal. This may be evidence that the hawkmoth elastically stores some negative power before beginning each stroke. Similar results were obtained by Wan *et al.* for the cicada [49]. Table III reports the cycle-averaged force and power for each flight speed. Since the hawkmoth was feeding occasionally during the recordings, the cycle-averaged lift presents a slight difference between different flight motions. According to our experimental measurements, the body weight of the hawkmoth was 14.2 mN before the recording, and 19.1 mN after all experiments. Table III also shows that the cycle-averaged mechanical power for hovering, and 2-m/s forward flight is greater than for 4-m/s forward flight. This can be explained by the reduction in drag from the wings as the hawkmoth's flying speed increases [see Figs. 12(e) and 12(f)]. During 4-m/s forward flight, the hawkmoth produces less drag than it does during hovering and 2-m/s forward flight, and as a result, its cycle-averaged mechanical power is lower. In addition, our results also shed the insights that the speed limit in hawkmoth forward flying seems not directly related to the high-power consumption in high-speed flight. This is consistent with a recent particle image velocimetry study of hawkmoth forward flight [53], which also found at the power requirements of flight at the maximum sustained wind tunnel flight speed was less than that of hovering flight.

Next, we compare the vortex structures generated by hawkmoth across three different flight speeds in Fig. 14. Five slides cut along the wingspan demonstrate how the different flapping kinematics modulate the LEV at various flight motions. During hovering flight, a strong LEV is formed and attached well on the wing surface during both the downstroke and the upstroke. At both forward flying speeds, a larger LEV is present during the downstroke (e.g., at $t/T = 0.25$ in Fig. 14), and a smaller LEV is present during the upstroke (e.g., at $t/T = 0.75$ in Fig. 14). To take a closer look at LEV formation with different flight motions, we present both three-dimensional and two-dimensional (2D) views of slice cuts at the middownstroke (Fig. 15) and midupstroke (Fig. 16).

Figure 15 depicts the vortex structures at $t/T = 0.25$, and it includes vectors to show the direction of net force at different forward flying speeds during the hawkmoth's downstroke. This figure shows that as the hawkmoth's flight speed increases, the net force vector during the downstroke becomes increasingly vertical. As a result, the drag produced during the downstroke is minimized as shown graphically in Fig. 12(f). We hypothesize that this minimization of drag may be attributed to flight stability requirements at higher forward flying speeds. The instantaneous momentum at higher flying speed is much higher than that at lower speed. So, the hawkmoth not only needs to maintain a cycle-averaged force balance in the horizontal direction, but also has to minimize the magnitude of drag force oscillation during each stroke. At higher flight speeds, the hawkmoth must limit instantaneous drag force magnitude during its downstroke to keep itself from blowing away in the incoming flow. In order to do so, the hawkmoth must keep its wing pitching angle roughly parallel to the incoming flow when flying at higher forward flight speeds as seen in Fig. 11(c).
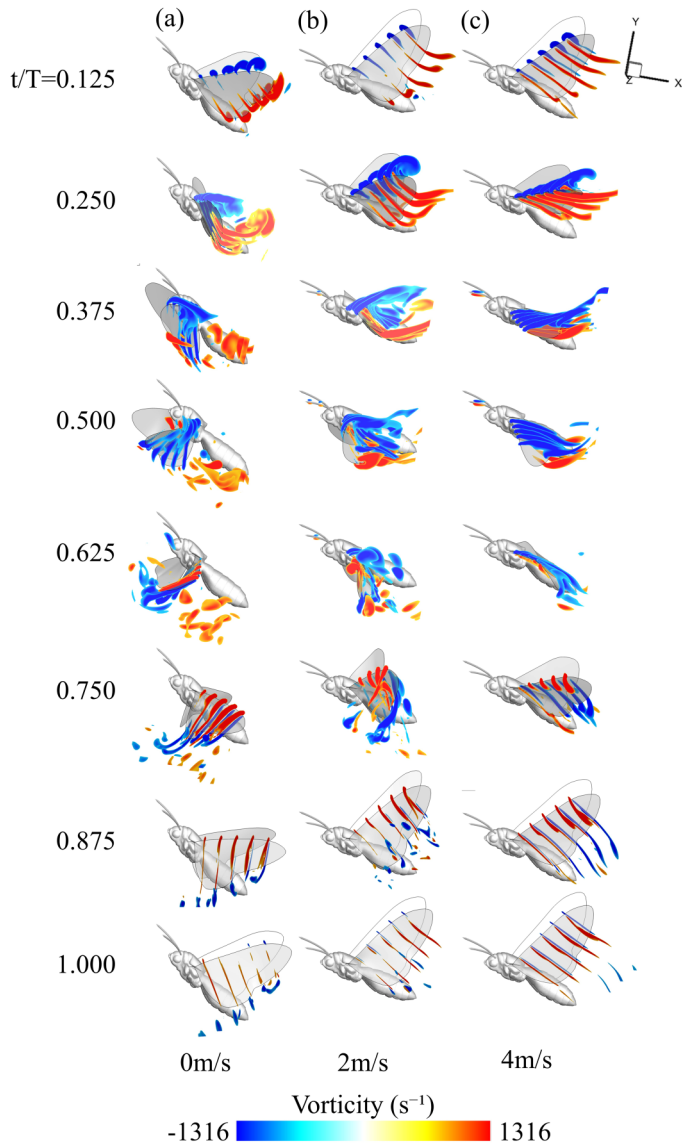
FIG. 14. Wing slices throughout one wingbeat cycle for (a) hawkmoth hovering, (b) 2-m/s forward flight, and (c) 4-m/s forward flight. A total of five slices were taken at 0.11R, 0.28R, 0.44R, 0.60R, and 0.77R.

Figure 16 shows the midupstroke vortex structures and net force vectors for hovering 2-m/s forward flight and 4-m/s forward flight. During the hovering upstroke, the wing pitch angle is more vertical, and the net force is angled upward. During the forward flight upstroke, however, the wing pitch angle is more horizontal, and the net force vector is angled down. As a result, lift is generated during the hovering upstroke but not during the forward flight upstroke, as shown graphically in Figs. 12(a)–12(c). We hypothesize that due to biological limitations, a hawkmoth cannot drastically alter its wing kinematics as it transitions from downstroke to upstroke. As a result, the horizontal wing orientation observed during a forward flying hawkmoth's downstroke is also present during its upstroke. This may explain why the hawkmoth's upstroke is used to generated positive lift during
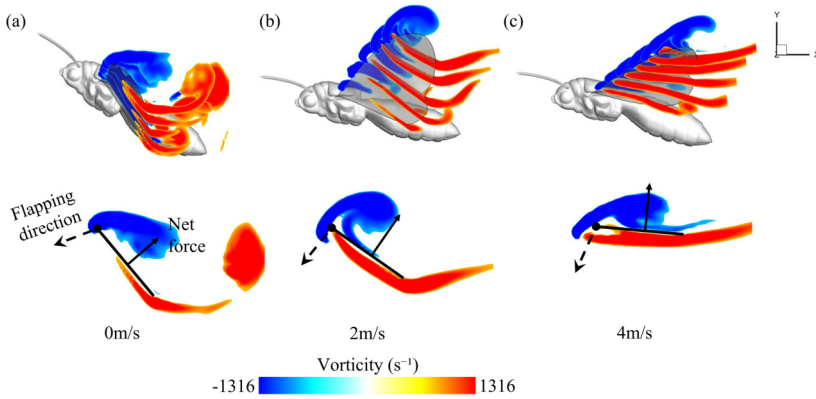
FIG. 15. Three-dimensional and two-dimensional views of slice cut vortex structures at middownstroke ($t/T = 0.25$) for (a) hawkmoth hovering, (b) 2-m/s forward flight, and (c) 4-m/s forward flight. The 2D view is shown for the chord located at $0.60R$. Net force vectors and arrows representing flapping direction are also included. The black circle is located along the wing's leading edge.

hovering flight but a significant amount of negative lift force generation was observed during 2- and 4-m/s forward flight.

Among all three simulations, we observed two separate LEV above the hawkmoth wing at 2-m/s forward flight as shown in Fig. 17. This phenomenon is also known as a dual LEV and has been observed throughout 1- and 2-m/s hawkmoth flight by Johansson *et al.* [54]. For the current paper, the dual LEV was only visible during the upstroke for the 2-m/s forward flying hawkmoth, but not for the 4-m/s case.

In addition to the visualization of the vortex structures near the wing surface, we also present the far wake structures. Figure 18 shows the time sequence for the flow field at hovering, 2-m/s forward flight and 4-m/s forward flight. The vortex structures were plotted using the isosurface of the Q criterion. For each flight speed, a strong LEV is formed during the downstroke. A tip vortex (TV) and trailing edge vortex (TEV) can also be observed. As one can expect, the downwash is located
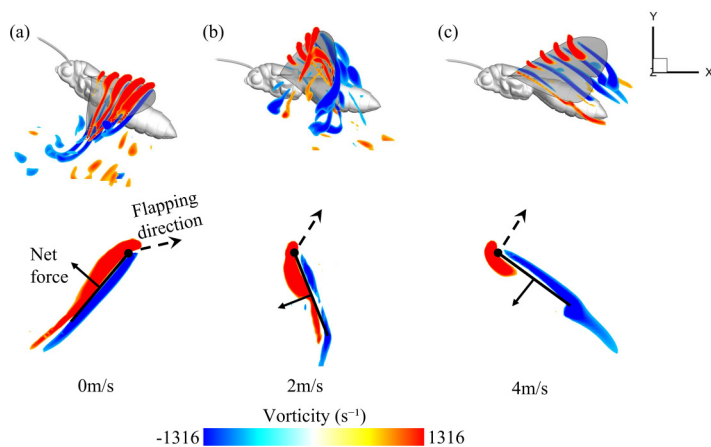

FIG. 16. Three-dimensional and two-dimensional views of slice cut vortex structures at midupstroke ($t/T = 0.75$) for (a) hawkmoth hovering, (b) 2-m/s forward flight, and (c) 4-m/s forward flight. The 2D view is shown for the chord located at $0.60R$. Net force vectors and arrows representing flapping direction are also included. The black circle is located along the wing's leading edge.
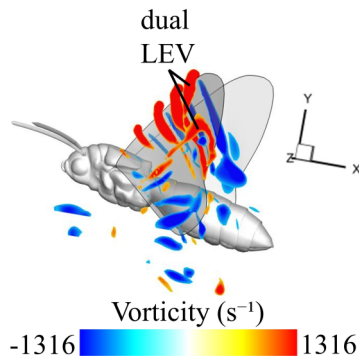
FIG. 17. Dual LEV is observed for the hawkmoth forward flight at 2-m/s forward flight. The time instant for this picture is at $t/T = 0.79$, around the midupstroke.

directly below the hawkmoth's body during hawkmoth hovering flight. At 2-m/s forward flight, the downwash is situated both below and behind the hawkmoth. When the flight speed increase to 4 m/s, a chain of vortex tubes is observed behind the insect body. This change in wake structures can be explained by a combination of flight speed and the induced flow generated by flapping wings at each flight speed. As the hawkmoth's flight speed increases, the wing kinematics shift from a back-and-forth motion to an up-and-down motion. During 4-m/s forward flight, the hawkmoth's wing pitching angle is roughly parallel to the incoming flow. Combined with such a high forward flying speed, vortices are shed directly behind the hawkmoth.

Figure 19 shows the vortex structures present at middownstroke ($t/T = 0.25$) for hovering, 2-m/s forward flight and 4-m/s forward flight. The downstroke for all three flight speeds is accompanied by the formation of a large LEV and TV. A TEV is also present during the downstroke for all three flapping cases. However, for 4-m/s forward flight, the size of the TEV is significantly smaller than for hovering and 2-m/s forward flight. Zheng *et al.* [15] and Aono *et al.* [14] have noted that during hovering flight, the LEV, TV, and TEV form a horseshoe-shaped pattern around the hawkmoth wing during the downstroke. For the current study, this pattern can be clearly observed during hovering and 2-m/s flight, but the much smaller TEV for 4-m/s flight prevents the formation of a full horseshoe pattern. This can be partially explained by the stretching and distortion of the vertex structures due to the strong convection at 4 m/s.

Next, we visualize the distribution of lift force generation on the wing surface. Figure 20 shows mean lift production on the wing surface during the downstroke and upstroke, respectively, for all simulated flight motions. Lift production during the hovering downstroke increases along the wingspan with the highest amount of lift produced near the wing tip and the lowest lift produced near the wing root. However, during the downstroke for the forward flying cases, the greatest lift is produced along the leading edge of the wing, and the lowest lift is produced along the trailing edge. We believe that this difference is linked to the location of the maximum flow velocity for each flight case. During hovering flight, the maximum flow velocity is generated by the wing tip, resulting in the greatest lift generation near this region. However, during forward flight, the flapping wing encounters the incoming flow which will enhance the development of the LEV along the wingspan. In addition, as the flying speed gradually increases, hawkmoths tilt the stroke plane more vertically, which further promotes lift generation during the downstroke. As a result, there is a larger LEV along the spanwise portion of the wing, and a greater portion of the overall lift is generated during the forward flight downstroke.

The most significant difference in the lift generation between hovering and forward flight appears during the upstroke. The hovering upstroke is similar to the hovering downstroke with lift production increasing along the wingspan, resulting in greatest lift close to the wing tip. However, the lift production during the forward flight upstroke displays an opposite pattern. For 2- and 4-m/s forward
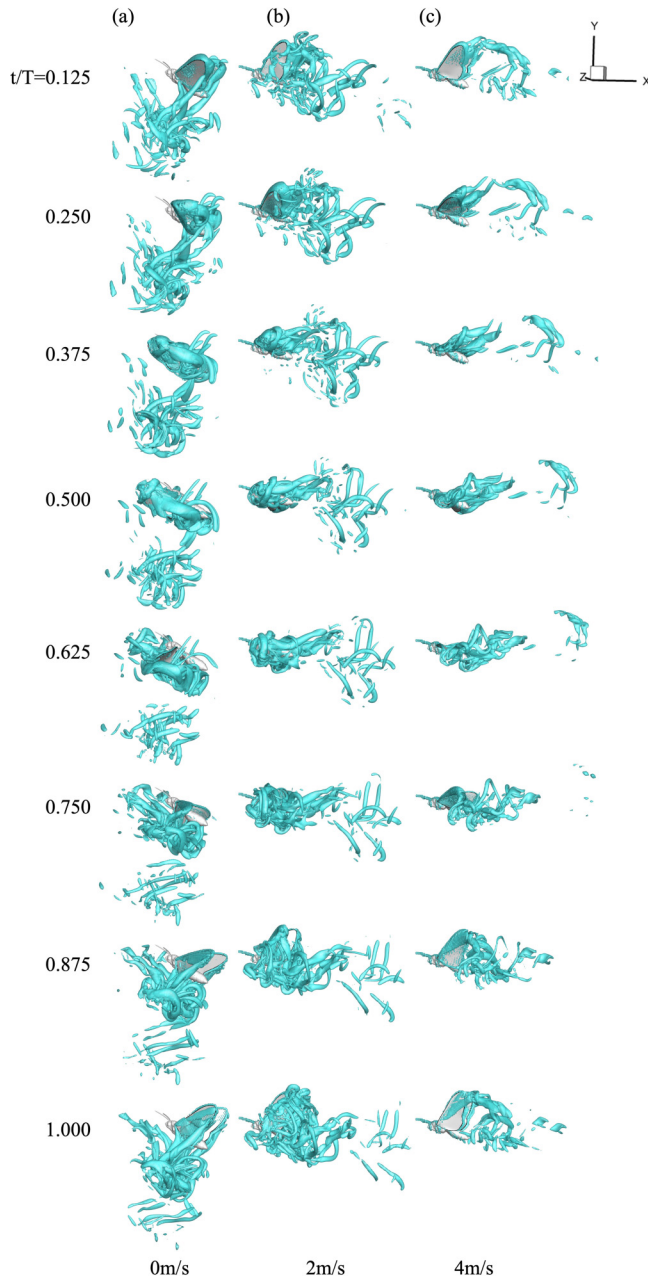
FIG. 18. Q-criterion vortex structures for (a) hawkmoth hovering, (b) 2-m/s forward flight, and (c) 4-m/s forward flight. The isosurface of $Q = 10(\overline{U}_{\text{tip}}/R)^2$ was used to plot the vortex structures. See movie 1 in the Supplemental Material for simulated flow animations [21].

flight, significant negative lift is produced near the wing tip, and a slight amount of positive lift production is seen close to the wing root. This reversal of lift production during the upstroke is evidence for a different mechanism of lift production for hovering compared to forward flight. For both 2- and 4-m/s forward flight, approximately 75% of the wing surface produces negative lift during the upstroke. This observation is reflected in Figs. 12(b) and 12(c), which shows positive
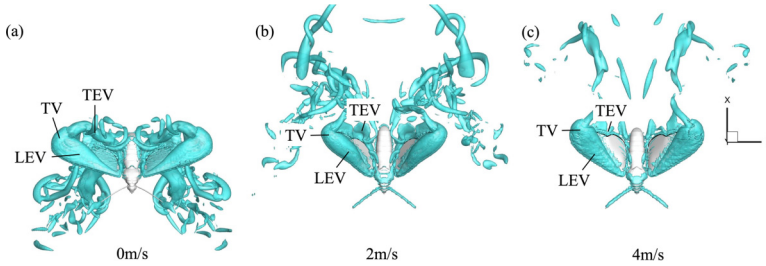
FIG. 19. Top view of vortex structure generated at the middownstroke ($t/T = 0.25$) for (a) hawkmoth hovering, (b) 2-m/s forward flight, and (c) 4-m/s forward flight. The isosurface of $Q = 10(\overline{U}_{\text{tip}}/R)^2$ was used to plot the vortex structures.

lift generation during the downstroke and negative lift generation during the upstroke for both 2- and 4-m/s forward flights. However, during the hovering upstroke, the entire wing surface shows positive lift production. This corresponds to Fig. 12(a), which shows that positive lift is generated during both the upstroke and downstroke for hovering flight.

C. Comparison of hawkmoths and other flying animals

We have observed that as the hawkmoth's advance ratio J increases along with flight speed, lift production is increasingly dominated by the downstroke. At hovering ($J = 0$), both the downstroke and upstroke provide positive contributions to the total lift generation for the flapping cycle. However, at 2-m/s ($J = 0.41$) and 4-m/s ($J = 0.85$) forward flight, the downstroke produces 100% of the overall lift, and negative lift is generated during the upstroke.

Several previous studies [2,3,49,55] have also commented on the relationship between an insect's advance ratio and the downstroke's contribution to total lift production. The results of the current paper are qualitatively consistent with results obtained by Sun and Wu [55] for a model fruit fly. They found that for an advance ratio of 0.13, the downstroke contributes 75% of the total lift production. For an advance ratio of 0.53, the downstroke contributes 100% of the total lift, and negative lift is generated during the upstroke. Dudley and Ellington [3] also found that for a relatively high advance ratio of 0.59, 100% of a bumblebee's total lift is produced during the downstroke, but they did not indicate whether the upstroke generates negative lift in their paper.

Following the definition presented in the literature [3], we evaluated the percentage of the vertical force generated during the downstroke ($F_{\text{vert,d}}$) over the vertical force generated during the entire cycle (F_{vert}) as a function of the advance ratio (J) across different species. Figure 21 shows the
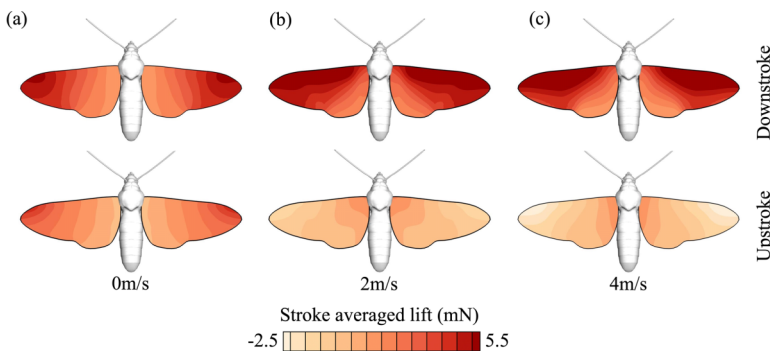

FIG. 20. Stroke-averaged lift force distribution on the wing surfaces during downstroke and upstroke for (a) hovering, (b) 2-m/s forward flight, and (c) 4-m/s forward flight.
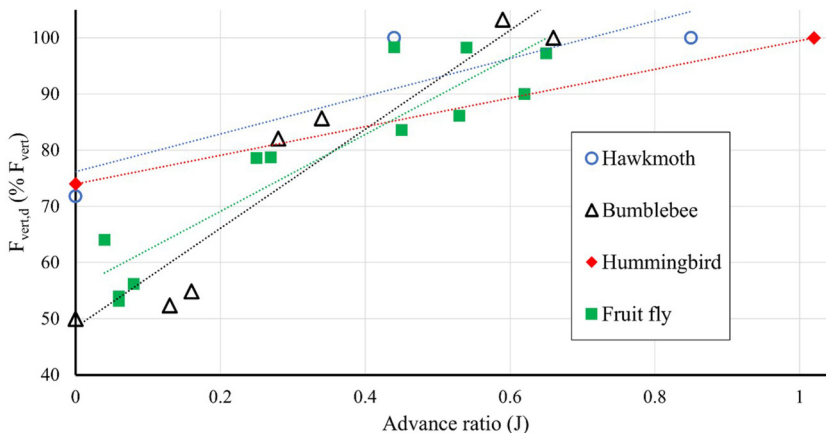
FIG. 21. Relationship between the advance ratio (J) and $F_{\text{vert,d}}$ (% F_{vert}) for different small animal species, including hawkmoth (current study), bumblebee [2,3], hummingbird [5,6], and fruit fly [4]. Least-squares trendlines are shown as dashed lines for each species.

relationship between J and $F_{\text{vert,d}}$ (% F_{vert}) for a variety of small flying animals. This plot shows that as an animal's advance ratio increases, the downstroke plays an increasingly important role in the overall lift production. The plot also shows that if the advance ratio is sufficiently high, the downstroke generates 100% of the total lift. In addition, a least-squares trendline is included for each species. Comparing the results for each species shows that as a flying animal's weight increases, the slope of this trendline generally decreases.

Based on the results from the current paper, we suspect that maximum flying speed limitation is due to changes in a flying animal's wing kinematics as its advance ratio increases. As the flight speed gradually increases, the animal must find a way to minimize drag during its entire flapping cycle to prevent itself from blowing away in the incoming flow. To minimize the magnitude of the instantaneous drag force generated during the downstroke, the animal has to reduce its wing pitching angle by orienting its wings roughly parallel to the flow direction, while still maintaining sufficient angle of attack for lift generation. As the advance ratio continuously increases with flight speed, a significant amount of negative lift force starts to appear during the upstroke resulting from a negative angle of attack. As a consequence, the positive lift generated during the animal's downstroke is not sufficient to overcome the body weight together with the negative lift generated during the upstroke. However, increasing downstroke lift would also increase downstroke drag, requiring more upstroke thrust and resulting in more upstroke negative lift. Thus, these kinematic limitations result in a limit to its maximum forward flying speed as we and others observe in wind tunnel flight studies [11,12]. Compared to birds and bats, insects are more strongly limited by these effects because they cannot reconfigure their wings during the stroke cycle. For example, birds typically flex their wings at the wrist joint during the upstroke, reducing wing span and area [56]. Despite having inflexible wings in comparison to most other bird species, even hummingbirds exhibit such an ability and increasingly reduce wing span during the upstroke as flight speed increases [57]. Insects have no such ability and, thus, might generally exhibit lower maximum flight speeds than flying vertebrates of similar wing loading.

IV. CONCLUSIONS

We have numerically investigated the unsteady aerodynamics of hawkmoth flight across a range of flying speeds (0–4 m/s). Flapping wing kinematics of hawkmoths have been reconstructed using high-speed wind tunnel recordings. An in-house immersed-boundary-method-based CFD solver

has been used to simulate hawkmoth's flight. Results show that as the hawkmoth transitions from hovering to forward flight, the hawkmoth's stroke plane angle increases and its upstroke wing pitch angle decreases. These kinematic changes lead to differences in aerodynamic force production and power consumption between hovering and forward flight.

During hawkmoth hovering, significant lift is generated during both the downstroke and upstroke with the downstroke contributing around 72% of the total lift. At 2- and 4-m/s forward flight, however, the downstroke provides all of the lift, and negative lift is generated during the upstroke. Detailed analysis has been performed on the vortex formation and force destructions on the wing surfaces. Our results indicated that the power consumption seem not to restrict forward flight speed in hawkmoths. Instead, the hawkmoth has to manage drag during its downstroke to prevent large, unstable body oscillations at higher forward flying speeds. To reduce drag force generated during each downstroke, the forward flying hawkmoth must maintain a small wing pitching angle that is roughly parallel to the flying direction. Due to biological limitations, the hawkmoth cannot drastically alter its wing pitching angle during the short period of the wing reversal. As a result, a forward flying hawkmoth's wings have to remain approximately horizontal with respect to the stroke plane during the upstroke, which leads to a negative lift force generation. As the flying speed increases, the lift generated during the downstroke cannot balance with the body weight together with the negative lift generated during the upstroke. This effect limits high speed flight in hawkmoths, and highlights the importance of reconfigurable wings to the wide range of flight speeds achieved by flying vertebrates.

---

[1] C. P. Ellington, C. van den Berg, A. P. Willmott, and A. L. R. Thomas, Leading-edge vortices in insect flight, Nature (London) **384**, 626 (1996).

[2] R. Dudley and C. Ellington, Mechanics of forward flight in bumblebees: I. Kinematics and morphology, J. Exp. Biol. **148**, 19 (1990).

[3] R. Dudley and C. Ellington, Mechanics of forward flight in bumblebees: II. Quasi-steady lift and power requirements, J. Exp. Biol. **148**, 53 (1990).

[4] H. J. Zhu and M. Sun, Kinematics measurement and power requirements of fruitflies at various flight speeds, Energies **13**, 4271 (2020).

[5] J. Song, H. Luo, and T. L. Hedrick, Three-dimensional flow and lift characteristics of a hovering ruby-throated hummingbird, J. R. Soc., Interface **11**, 20140541 (2014).

[6] J. Song, B. W. Tobalske, D. R. Powers, T. L. Hedrick, and H. Luo, Three-dimensional simulation for fast forward flight of a calliope hummingbird, R. Soc. Open Sci. **3**, 160230 (2016).

[7] D. R. Warrick, B. W. Tobalske, and D. R. Powers, Aerodynamics of the hovering hummingbird, Nature (London) **435**, 1094 (2005).

[8] K. Suzuki, K. Minami, and T. Inamuro, Lift and thrust generation by a butterfly-like flapping wing–body model: Immersed boundary–lattice boltzmann simulations, J. Fluid Mech. **767**, 659 (2015).

[9] T. L. Hedrick and T. Daniel, Flight control in the hawkmoth manduca sexta: The inverse problem of hovering, J. Exp. Biol. **209**, 3114 (2006).

[10] R. Stevenson, K. Corbo, L. Baca, and Q. Le, Cage size and flight speed of the tobacco hawkmoth manduca sexta, J. Exp. Biol. **198**, 1665 (1995).

[11] A. P. Willmott and C. P. Ellington, The mechanics of flight in the hawkmoth manduca sexta. I. Kinematics of hovering and forward flight, J. Exp. Biol. **200**, 2705 (1997).

[12] T. L. Hedrick, J. Martínez-Blat, and M. J. Goodman, Flight motor modulation with speed in the hawkmoth manduca sexta, J. Insect Physiol. **96**, 115 (2017).

[13] A. P. Willmott and C. P. Ellington, The mechanics of flight in the hawkmoth manduca sexta. II. Aerodynamic consequences of kinematic and morphological variation, J. Exp. Biol. **200**, 2723 (1997).

[14] H. Aono, W. Shyy, and H. Liu, Near wake vortex dynamics of a hovering hawkmoth, Acta Mech. Sin. **25**, 23 (2009).

[15] L. Zheng, T. L. Hedrick, and R. Mittal, A multi-fidelity modelling approach for evaluation and optimization of wing stroke aerodynamics in flapping flight, J. Fluid Mech. **721**, 118 (2013).

[16] J. Yao and K. S. Yeo, Forward flight and sideslip manoeuvre of a model hawkmoth, J. Fluid Mech. **896**, 361 (2020).

[17] V. M. Ortega-Jimenez, J. S. M. Greeter, R. Mittal, and T. L. Hedrick, Hawkmoth flight stability in turbulent vortex streets, J. Exp. Biol. **216**, 4567 (2013).

[18] D. H. Theriault, N. W. Fuller, B. E. Jackson, E. Bluhm, D. Evangelista, Z. Wu *et al.*, A protocol and calibration method for accurate multi-camera field videography, J. Exp. Biol. **217**, 1843 (2014).

[19] C. Koehler, Z. X. Liang, Z. Gaston, H. Wan, and H. B. Dong, 3D reconstruction and analysis of wing deformation in free-flying dragonflies, J. Exp. Biol. **215**, 3018 (2012).

[20] C. Li and H. Dong, Wing kinematics measurement and aerodynamics of a dragonfly in turning flight, Bioinspir. Biomim. **12**, 026001 (2017).

[21] See Supplemental Material at http://link.aps.org/supplemental/10.1103/PhysRevFluids.7.093104 for image-based flow simulation of hawkmoth in hovering and forward flight.

[22] R. Mittal, H. Dong, M. Bozkurttas, F. M. Najjar, A. Vargas, and A. von Loebbecke, A versatile sharp interface immersed boundary method for incompressible flows with complex boundaries, J. Comput. Phys. **227**, 4825 (2008).

[23] M. R. Visbal and D. V. Gaitonde, Very high-order spatially implicit schemes for computational acoustics on curvilinear meshes, J. Comput. Acoust. **9**, 1259 (2001).

[24] M. R. Visbal and D. Rizzetta, Large-Eddy simulation on curvilinear grids using compact differencing and filtering schemes, J. Fluids Eng. **124**, 836 (2002).

[25] M. R. Visbal and D. V. Gaitonde, On the use of higher-order finite-difference schemes on curvilinear and deforming meshes, J. Comput. Phys. **181**, 155 (2002).

[26] R. Löhner, *Applied Computational Fluid Dynamics Techniques: An Introduction Based on Finite Element Methods* (Wiley, Hoboken, NJ, 2008).

[27] T. E. Tezduyar, Finite element methods for fluid dynamics with moving boundaries and interfaces, in *Encyclopedia of Computational Mechanics* (Wiley, Hoboken, NJ, 2004).

[28] T. E. Tezduyar, S. Sathe, R. Keedy, and K. Stein, Space–time finite element techniques for computation of fluid–structure interactions, Comput. Meth. Appl. Mech. Eng. **195**, 2002 (2006).

[29] D. Goldstein, R. Handler, and L. Sirovich, Modeling a no-slip flow boundary with an external force field. Comput. Phys. **105**, 354 (1993).

[30] C. S. Peskin, Flow patterns around heart valves: A numerical method, J. Comput. Phys. **10**, 252 (1972).

[31] K. Taira and T. Colonius, The immersed boundary method: A projection approach, J. Comput. Phys. **225**, 2118 (2007).

[32] J. Kim, D. Kim, and H. Choi, An immersed-boundary finite-volume method for simulations of flow in complex geometries, J. Comput. Phys. **171**, 132 (2001).

[33] H. Dong, M. Bozkurttas, R. Mittal, P. Madden, and G. V. Lauder, Computational modeling and analysis of the hydrodynamics of a highly deformable fish pectoral fin, J. Fluid Mech. **645**, 345 (2010).

[34] T. Ye, R. Mittal, H. S. Udaykumar, and W. Shyy, An accurate cartesian grid method for viscous incompressible flows with complex immersed boundaries, J. Comput. Phys. **156**, 209 (1999).

[35] R. Mittal and G. Iaccarino, Immersed boundary methods, Annu. Rev. Fluid. Mech. **37**, 239 (2005).

[36] C. Li, H. Dong, and K. Zhao, A balance between aerodynamic and olfactory performance during flight in Drosophila, Nat. Commun. **9**, 3215 (2018).

[37] C. Li, Effects of wing pitch kinematics on both aerodynamic and olfactory functions in an upwind surge, Proc. Inst. Mech. Eng. Part C J. Mech. Eng. Sci. **235**, 296 (2021).

[38] C. Li, H. Dong, and K. Zhao, Dual functions of insect wings in an odor-guided aeronautic navigation, J. Fluids Eng. **142**, 030902 (2020).

[39] C. Li and H. Dong, Three-dimensional wake topology and propulsive performance of low-aspect-ratio pitching-rolling plates, Phys. Fluids **28**, 071901 (2016).

[40] C. Li, H. Dong, and B. Cheng, Tip vortices formation and evolution of rotating wings at low reynolds numbers, Phys. Fluids **32**, 021905 (2020).

[41] C. Li, J. Wang, G. Liu, X. Deng, and H. Dong, Passive Pitching Mechanism of Three-Dimensional Flapping Wings in Hovering Flight, in *Proceedings of the 8th Joint Fluids Engineering Conference on ASME-JSME-KSME 2019* (ASME, San Francisco, 2019), Paper No. AJKFluids2019-4639.

[42] M. Lei, J. P. Crimaldi, and C. Li, Navigation in odor plumes: How do the flapping kinematics modulate the odor landscape?, *AIAA Aviation 2021 Forum* (AIAA, Reston, VA, 2021), Paper No. AIAA 2021-2817.

[43] C. Li, H. Dong, and G. Liu, Effects of a dynamic trailing-edge flap on the aerodynamic performance and flow structures in hovering flight, J. Fluids Struct. **58**, 49 (2015).

[44] C. Li, J. Jiang, H. Dong, and K. Zhao, Computational modeling and validation of human nasal airflow under various breathing conditions, J. Biomech. **64**, 59 (2017).

[45] M. Lei and C. Li, The aerodynamic performance of passive wing pitch in hovering flight, Phys. Fluids **32**, 051902 (2020).

[46] A. Medina, J. D. Eldredge, J. Kweon, and H. Choi, Illustration of wing deformation effects in three-dimensional flapping flight, AIAA J. **53**, 2607 (2015).

[47] E. Dilek, B. Erzincanli, and M. Sahin, The numerical investigation of lagrangian and eulerian coherent structures for the near wake structure of a hovering drosophila, Theor. Comput. Fluid Dyn. **33**, 255 (2019).

[48] J.-S. Han, J. W. Chang, and J.-H. Han, The advance ratio effect on the lift augmentations of an insect-like flapping wing in forward flight, J. Fluid Mech. **808**, 485 (2016).

[49] H. Wan, H. Dong, and K. Gai, Computational investigation of cicada aerodynamics in forward flight, J. R. Soc., Interface **12**, 20141116 (2015).

[50] H. Aono and H. Liu, Vortical structure and aerodynamics of hawkmoth hovering, J. Biomechan. Sci. Eng. **1**, 234 (2006).

[51] Y. Z. Lyu and M. Sun, Power requirements for the hovering flight of insects with different sizes, J. Insect Physiol. **134**, 104293 (2021).

[52] G. Liu, H. Dong, and C. Li, Vortex dynamics and new lift enhancement mechanism of wing–body interaction in insect forward flight, J. Fluid Mech. **795**, 634 (2016).

[53] K. Warfvinge, M. KleinHeerenbrink, and A. Hedenström, The power–speed relationship is U-shaped in two free-flying hawkmoths (Manduca sexta), J. R. Soc., Interface **14**, 20170372 (2017).

[54] L. C. Johansson, S. Engel, A. Kelber, M. K. Heerenbrink, and A. Hedenström, Multiple leading edge vortices of unexpected strength in freely flying hawkmoth, Sci. Rep. **3**, 3264 (2013).

[55] M. Sun and J. H. Wu, Aerodynamic force generation and power requirements in forward flight in a fruit fly with modeled wing motion, J. Exp. Biol. **206**, 3065 (2003).

[56] B. Tobalske and K. Dial, Flight kinematics of black-billed magpies and pigeons over a wide range of speeds, J. Exp. Biol. **199**, 263 (1996).

[57] B. W. Tobalske, D. R. Warrick, C. J. Clark, D. R. Powers, T. L. Hedrick, G. A. Hyder *et al.*, Three-dimensional kinematics of hummingbird flight, J. Exp. Biol. **210**, 2368 (2007).